Molecules and Cells

Real-Time Measurement of the Liquid Amount in Cryo-Electron Microscopy Grids Using Laser Diffraction of Regular 2-D Holes of the Grids

Jinsook Ahn[1], Dukwon Lee[1], Inseong Jo[1,4], Hyeongseop Jeong[2,3], Jae-Kyung Hyun[2,5], Jae-Sung Woo[3], Sang-Ho Choi[1], and Nam-Chul Ha[1,*]

[1]Department of Agricultural Biotechnology, Center for Food Safety and Toxicology, Center for Food and Bioconvergence, and Research Institute for Agriculture and Life Sciences, CALS, Seoul National University, Seoul 08826, Korea, [2]Korea Basic Science Institute, Daejeon 28119, Korea, [3]Department of Life Sciences, Korea University, Seoul 02841, Korea, [4]Present address: KoBioLabs, Inc., Seoul 08826, Korea, [5]Present address: Molecular Cryo-Electron Microscopy Unit, Okinawa Institute of Science and Technology, Okinawa 904-0496, Japan
*Correspondence: hanc210@snu.ac.kr
https://doi.org/10.14348/molcells.2020.2238
www.molcells.org

Cryo-electron microscopy (cryo-EM) is now the first choice to determine the high-resolution structures of huge protein complexes. Grids with two-dimensional arrays of holes covered with a carbon film are typically used in cryo-EM. Although semi-automatic plungers are available, notable trial-and-error is still required to obtain a suitable grid specimen. Herein, we introduce a new method to obtain thin ice specimens using real-time measurement of the liquid amounts in cryo-EM grids. The grids for cryo-EM strongly diffracted laser light, and the diffraction intensity of each spot was measurable in real-time. The measured diffraction patterns represented the states of the liquid in the holes due to the curvature of the liquid around them. Using the diffraction patterns, the optimal time point for freezing the grids for cryo-EM was obtained in real-time. This development will help researchers rapidly determine high-resolution protein structures using the limited resource of cryo-EM instrument access.

Keywords: cryo electron microscopy, grid preparation, laser diffraction, real-time measurement, vitreous ice

INTRODUCTION

Cryo-electron microscopy (cryo-EM) has made spectacular advances and is now considered the first choice to determine the high-resolution structures of protein complexes in native states. The development of a direct electron detection camera was the primary trigger of the remarkable progress in single-particle cryo-EM in the last few years (Bai et al., 2015; Binshtein and Ohi, 2015; McMullan et al., 2014). New software for image processing and increased computing power-assisted by graphic processing units enable researchers to determine the structure in a reasonable time (Kimanius et al., 2016; Scheres, 2012). To visualize the native conformation of protein samples in the high vacuum inside the electron microscope and to reduce the radiation damage caused by electrons, the preparation of cryogenic sample grids is strictly required (Glaeser, 2008; Massover, 2011).

Although many experimental steps in the collection of EM images have been simplified and automated, the whole method is not routine or standardized compared to X-ray crystallography (Feng et al., 2017; Liu and Sigworth, 2014; Stagg et al., 2006). One of the limiting steps of cryo-EM is to

Received 21 October, 2019; revised 9 December, 2019; accepted 10 December, 2019; published online 9 March, 2020

eISSN: 0219-1032

reproducibly obtain a thin layer of the frozen aqueous solution from the grid (Glaeser et al., 2016). Typically, 2 to 5 μl of protein sample is loaded on the EM grid, and the excess sample liquid (~99.9% of the sample volume) is removed through blotting with a filter paper (Rubinstein et al., 2019). Although blotting force and time are adjustable in this procedure, they are typically not predictable for each grid preparation due to variable protein sample, concentration, and buffer composition (Noble et al., 2018). Thus, much trial-and-error practice interferes with efficient use of the expensive cryo-EM facility.

Recently, the use of self-blotting grids was introduced to allow cryo-grid preparation in combination with ink-jet spotting (Jain et al., 2012; Razinkov et al., 2016). More recently, a blot-free and lossless preparation from nanoliter-sized protein samples was developed (Arnold et al., 2017). Here, we present a new approach to monitor the states of liquid layers around the holes in EM grids using the diffraction of a laser beam by the EM grid.

MATERIALS AND METHODS

Apparatus

A prototype of the Diffracto-Plunger DP-2019A (XTEM BioLab, Korea; https://xtembiolab.com/) was used to measure the diffraction pattern and intensity and to prepare the cryo-EM grids by plunging into liquid ethane. A 5-mW, 650-nm red laser outfitted with a 5-mm-long collimator with a 5-mm hole was used as the light source.

Sample preparation

Prior to the use of the grids, the Quantifoil R1.2/1.3 grids (Pelco International, USA) were glow discharged for 50 s using a plasma cleaner (medium setting on Harrick module, PKC-3xG; Harrick Scientific Corp., USA). Distilled water (DW) was loaded on the Quantifoil grids and plunged into liquid ethane using the Diffracto-Plunger DP-2019A (XTEM BioLab) under 90% humidity.

EM images

The grids were imaged under low-dose conditions using a Titan Krios electron microscope (Thermo Fisher Scientific, USA) operated at 300 kV. The specimen stage was maintained at the temperature of liquid nitrogen. Images were recorded using a Falcon 3EC direct electron detector (Thermo Fisher Scientific).

RESULTS

Diffraction of a laser beam by cryo-EM grids with 2-dimensional arrays of holes

Quantifoil EM grids are widely used for cryo-EM and are covered with carbon film, which has a two-dimensional (2-D) array of holes on 300- to 400-mesh copper grids (Figs. 1A and 1B). Because the copper EM grids can act as a 2-D grating for a laser beam, a diffraction pattern can be obtained when, for example, a red laser (650-nm wavelength) is applied to

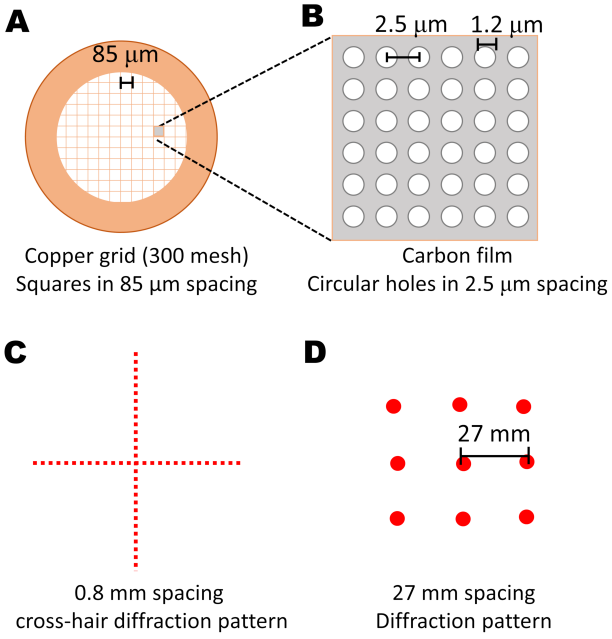

Fig. 1. Quantifoil grid (R1.2/1.3, 300-mesh copper grid) and its predicted diffraction patterns from a 650-nm laser beam at a 10-cm distance. (A) Schematic of a 300-mesh Quantifoil grid with 85-μm spacing. (B) Enlarged schematic view of the holes in the carbon film, with the diameter and spacing of the holes, was indicated. (C) The calculated diffraction pattern of a 300-mesh square grid at a 10-cm distance using a 650-nm laser beam. (D) The calculated diffraction pattern of the 2.5-μm spacing of the circular holes.

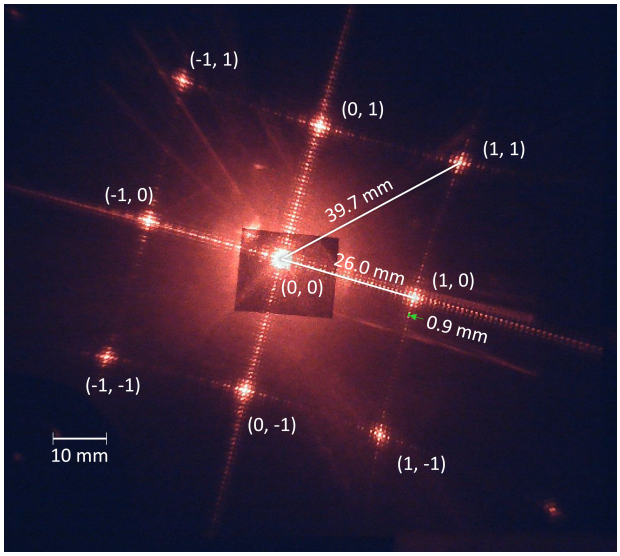

Fig. 2. A representative diffraction image of a Quantifoil grid (R 1.2/1.3, 300-mesh copper grid) at a 10-cm distance from the screen using laser light at 650 nm. Rectangular black tape was attached to reduce the intensity of the direct beam (0, 0). The cross-hair line with 0.9-mm spacing (green arrow) is due to the 300-mesh copper grid. The indexed spots from the holes in the carbon film on the grid were represented.

a 300-mesh grid (Fig. 1). Despite the presence of the carbon film on the copper grid, the laser beam partially penetrates the thin film to produce a diffraction pattern that can be calculated using Bragg's law, $n\lambda = 2d \sin\theta$, where n is an integer, d is the spacing between reflection planes, and θ is the reflection angle. The 85-μm squares in the 300-mesh copper grid generate a cross-hair diffraction pattern with 0.8-mm spacing on a screen at a 10-cm distance from the grid (Fig. 1C). The square shape of the mesh produces strong diffractions along the x- and y-axes of the mesh, while diffraction in the other directions is weakened by cancelation, which is correlated with the point spread function of the square. Importantly, there is another level of regularity in the holes of the carbon film (Fig. 1B). The Quantifoil R1.2/1.3 grid has 2.5-μm spacing between the centers of 1.2-μm-diameter holes on a 300-mesh copper gird (Pelco International). The circular holes of the carbon film laid on the copper grid generate a grid diffraction pattern with 27-mm spacing (Fig. 1D).

In the diffraction experiment, the grid strongly diffracted the 650-nm laser beam (Fig. 2), resulting in a noticeable central cross-hair pattern with 0.9-mm spacing. The spacing of the diffraction pattern was consistent with the 0.8-mm value calculated from the 85-μm spacing (pitch) of the 300-mesh grid. Another diffraction pattern with much longer spacing was observed in addition to the central cross-hair pattern (Fig. 2). The 26-mm spacing of this diffraction image coincided with the 27-mm value calculated from the 2.5 μm between the holes of the grids. The diffraction spots exhibited a further fine structure of a cross-hair pattern because the holes were under the background of the 300-mesh grid (Fig. 2). Theoretical analysis showed that each spot was a convolution of the two regularities of the grids, and the diffraction images represent the Fourier-transformed images of the grids.

Device architecture

To analyze the correlation between the liquid amount on the grid and diffraction pattern, we designed a custom equipment assembly, a schematic of which is presented in Fig. 3. A dark chamber with a distance of 10-cm from the grid to screen contains a laser/filter paper assembly that moves horizontally to allow loading of the sample liquid at the retracted position (R; Fig. 3A) and absorption of the sample liquid with the filter paper at the absorption position (A; Fig. 3B). The diffraction image is collected when a circular filter paper with a "V" shape is at position R, and the filter paper at position A absorbs the sample liquid on the grid (Fig. 3C). The camera records the diffraction images, and a Cadmium sulfide (CdS) based light sensor measures the beam intensities of the diffraction spots from the Quantifoil holes during the absorption step. Because the CdS-based light sensor provides a log-scale value for light intensity due to its electronic properties, the measured values are more sensitive at lower light intensities. Therefore, the value measured by the CdS-based light sensor will hereafter be used as the light intensity despite the technical differences between the two values.

Volume-based changes in the diffraction pattern

Prior to loading the sample on the grid, we measured the intensity of the diffraction spot for an empty grid. The sample was then loaded with the laser/filter paper assembly at the retracted position. As soon as the filter paper touched the grid (by approaching the laser/filter paper assembly), the diffracted beam intensity was recorded; the process was also documented on video (Fig. 4, Supplementary Video S1). Most of the liquid on the grid was absorbed by the filter paper at the same time as contact (Fig. 4; a). After an initial lag of 7 s (Fig. 4; a-c), a gradually decreased diffraction intensity was observed over 30-40 s (Fig. 4; c-e). At approximately 35 s, the minimum diffraction intensity was recorded with blurred diffraction spots (Fig. 4; e). The intensity then increased with a steep slope for approximately 20 s, followed by a more mild increase (Fig. 4; e-g) until the diffraction intensity matched

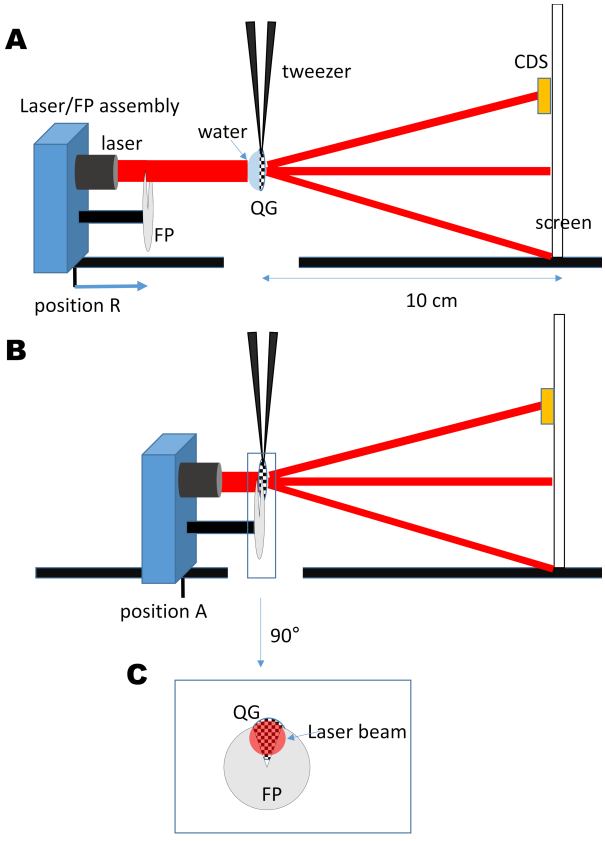

Fig. 3. Schematic of the plunging apparatus. The laser/filter paper (FP) assembly moves between the 'R' and 'A' positions. The laser (red line or red circle) is aligned horizontally to the Quantifoil grid (QG), which is affixed using a sharp tweezer. The diffraction spots appear on the screen, and the CdS light sensor measures the light intensity of a spot in real-time. (A) In the 'R' position, the light intensity of the spot from the empty QG is recorded, and then the sample is loaded onto the QG. (B) The laser/FP assembly is moved to the 'A' position. The FP, cut into a V-shape, absorbs the liquid on the QG at time 0. Then, the graph showing the light intensity of the spot is produced for the time course. (C) Alignment of the QG, the V-cut filter paper, and the laser beam. The laser beam passes through space in the V-cut filter paper and irradiates the QG.

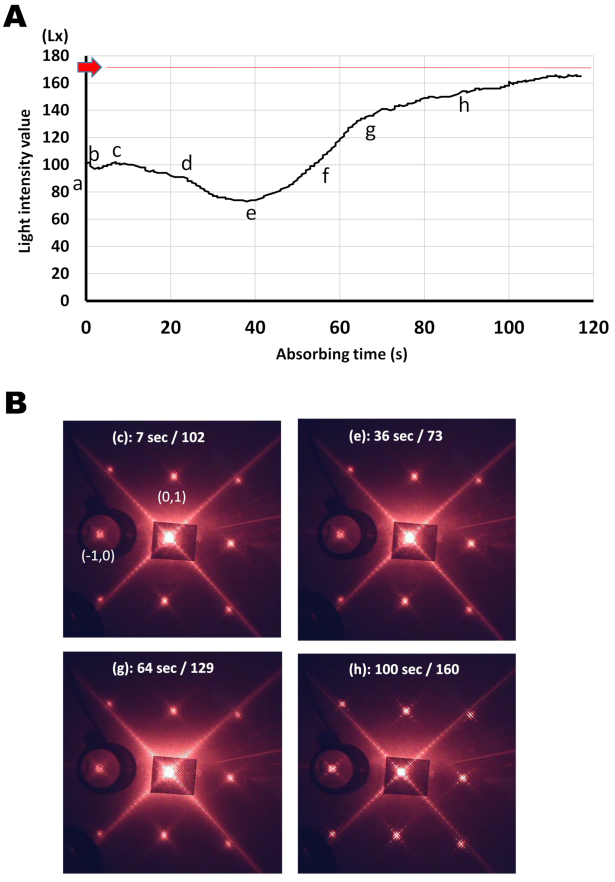

Fig. 4. Changes in diffraction patterns when pure water is loaded on the grids. (A) The time-dependent light scattering profiles of DW. One diffraction spot (-1, 0) was recorded using the CdS-based sensor and is circled in the image (B). The light intensity value was represented as Lx, which is arbitrary units. Time 0 is when the laser/filter paper module contacted the grid. The initial light intensity was represented as a red arrow. The image at (a) shows the diffraction image of the empty grid. (B) The diffraction patterns of DW at the time points (c, e, g, and h) denoted in (A).

that of the empty grid (Fig. 4; h).

Although significant variations were observed in the time required to reach the minimum light intensity, each grid showed a similar pattern of time-dependent diffraction light change in terms of the direction of change (i.e., increased or decreased). Therefore, the state of the liquid on the grid could be determined by carefully monitoring the decrease and/or increase in light intensity. Because the device was also equipped with a plunging apparatus, the grids were plunged at the desired time point, which was determined based on diffraction intensity. Optimal ice thickness was typically obtained when the grids were prepared in the steeply increasing region (Fig. 4; e-g), which was highly reproducible (Fig. 5). Of the 6 grids prepared in the steeply increasing region, all showed a reasonable ice thickness (Supplementary Fig. S1).

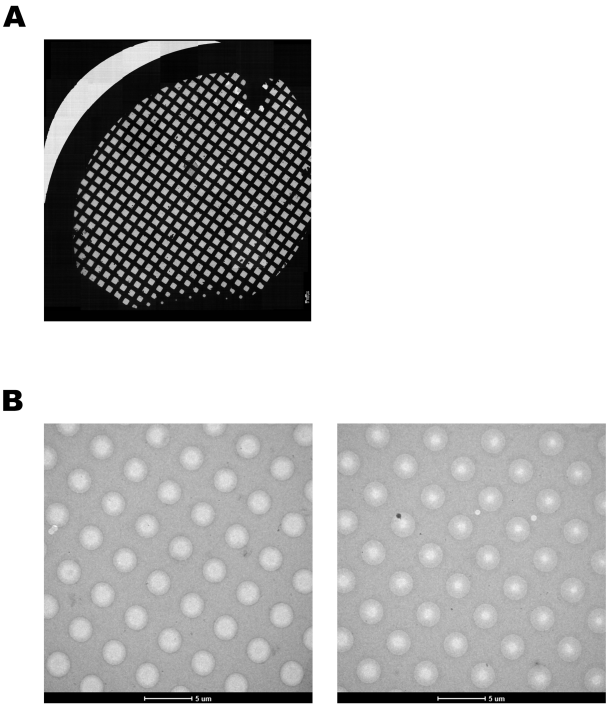

Fig. 5. Overall atlas of the grid showing a vitrified sample on a Quantifoil grid. (A) Representative grid atlas collected using EPU (Thermo Fisher Scientific) showing constant ice thickness in most of the grid squares. (B) TEM images of holey carbon grids with embedded vitreous ice.

DISCUSSION

Diffraction patterns provide Fourier-transformed information on the regularities. In preparing EM grids, it is helpful to know the liquid amounts on the grid in real-time. Although high-end light microscopy at high magnification could provide this information, it would be impossible to determine the state of the entire grid because only a small area can be visualized in real-time at high magnification. In contrast, diffraction images show the overall feature of the grid states in a cost-effective manner because each diffraction spot is a summation of the light from all the holes using an inexpensive laser source. Thus, the diffraction method might yield better information on the grid states, allowing researchers to determine suitable conditions for each cryo-EM experiment at an affordable price.

There are many factors affecting the intensities and shapes of diffraction patterns. It is reasonable to assume that the depth of the liquid in the holes does not decrease the penetration efficiency of the laser light because the liquid layer is extremely thin compared to the distance to the screen and does not highly absorb laser light at 650 nm. However, backscattering at the incidence of the beam on the surface of the liquid should be taken into consideration. The backscattering of light would decrease the penetration rate of the laser even though the liquid layer in the holes is very thin. The penetration efficiency would be fully recovered when the liquid layers were removed by complete drying.

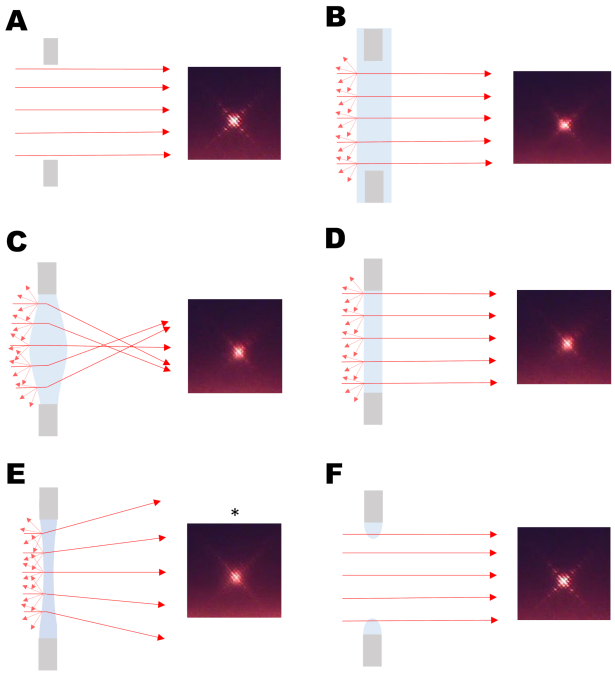

Fig. 6. Interpretation of liquid amounts in holes and diffraction images. (A-F) The predicted liquid curvature in the hole that affects the diffraction patterns over blotting time. The hypothetical liquid amounts in the holes for each diffraction image (right) are represented on the left. The diffracted reflection was produced when the laser faced another medium. The refraction patterns of the laser were used to determine the curvature of the liquid in the holes. Gray squares represent the ends of the holes in the Quantifoil grid, and blue represents water.

Another important factor is the refraction of light by the liquid layer, as light is refracted differently by concave and convex shapes. The curvature of the liquid in the grid holes is changed depending on the amount and surface tension of the liquid. If the liquid curvature is convex appropriately, the diffraction beam would be focused on the screen leading to a slight increase in the diffraction intensity. If the liquid curvature is concave, the diffracted light diverges on the screen or the light sensor, resulting in blurred diffraction spots with decreased diffraction intensities. Indeed, a slightly elevated diffraction intensity was observed within 7 s, which might be related to the convex curvature of the liquid in the holes (Figs. 4A; c and 6C). Then the diffraction intensities were decreased as the filter paper absorbed the sample liquid (Fig. 4; e), which would be associated with the concave shape of the liquid in the holes as shown in Fig. 6E. As the filter paper absorbs more liquid from the grid, the water membrane formed by the concave curvature in the holes would be ruptured, which increases the diffraction intensity (Fig. 6F). In this study, the time between minimum diffraction intensity and the increasing-intensity region was suitably discernable to allow for the plunging of the grids into the liquid ethane at that time point.

Based on these preliminary data, we are preparing grids with protein samples to collect images for structural determination. We believe that the real-time monitoring of grid states using the diffraction method will reduce EM time by allowing rapid determination of the optimal conditions for reproducible freezing.

Note: Supplementary information is available on the Molecules and Cells website (www.molcells.org).

Disclosure

The authors have no potential conflicts of interest to disclose.

ACKNOWLEDGMENTS

This research was supported by the Korea Institute of Planning and Evaluation for Technology in Food, Agriculture, and Forestry (IPET; 710012-03-1-HD120; ARC program to NCH), funded by the Ministry of Agriculture, Food, and Rural Affairs. This study was also supported by grants from the National Research Foundation of Korea (NRF-2017R1A2B2003992 and NRF-2017M3A9R6029755 to NCH).

ORCID

Jinsook Ahn https://orcid.org/0000-0002-4175-5181
Dukwon Lee https://orcid.org/0000-0003-2733-1953
Inseong Jo https://orcid.org/0000-0002-7964-4751
Hyeongseop Jeong https://orcid.org/0000-0003-0095-3402
Jae-Kyung Hyun https://orcid.org/0000-0003-2914-537X
Jae-Sung Woo https://orcid.org/0000-0001-9163-3433
Sang-Ho Choi https://orcid.org/0000-0003-3865-1039
Nam-Chul Ha https://orcid.org/0000-0003-4813-748X

REFERENCES

Arnold, S.A., Albiez, S., Bieri, A., Syntychaki, A., Adaixo, R., McLeod, R.A., Goldie, K.N., Stahlberg, H., and Braun, T. (2017). Blotting-free and lossless cryo-electron microscopy grid preparation from nanoliter-sized protein samples and single-cell extracts. J. Struct. Biol. *197*, 220-226.

Bai, X.C., McMullan, G., and Scheres, S.H. (2015). How cryo-EM is revolutionizing structural biology. Trends Biochem. Sci. *40*, 49-57.

Binshtein, E. and Ohi, M.D. (2015). Cryo-electron microscopy and the amazing race to atomic resolution. Biochemistry *54*, 3133-3141.

Feng, X., Fu, Z., Kaledhonkar, S., Jia, Y., Shah, B., Jin, A., Liu, Z., Sun, M., Chen, B., and Grassucci, R.A. (2017). A fast and effective microfluidic spraying-plunging method for high-resolution single-particle cryo-EM. Structure *25*, 663-670.e3.

Glaeser, R.M. (2008). Retrospective: radiation damage and its associated "information limitations". J. Struct. Biol. *163*, 271-276.

Glaeser, R.M., Han, B.G., Csencsits, R., Killilea, A., Pulk, A., and Cate, J.H. (2016). Factors that influence the formation and stability of thin, cryo-EM specimens. Biophys. J. *110*, 749-755.

Jain, T., Sheehan, P., Crum, J., Carragher, B., and Potter, C.S. (2012). Spotiton: a prototype for an integrated inkjet dispense and vitrification system for cryo-TEM. J. Struct. Biol. *179*, 68-75.

Kimanius, D., Forsberg, B.O., Scheres, S.H., and Lindahl, E. (2016). Accelerated cryo-EM structure determination with parallelisation using GPUs in RELION-2. Elife *5*, e18722.

Liu, Y. and Sigworth, F.J. (2014). Automatic cryo-EM particle selection for membrane proteins in spherical liposomes. J. Struct. Biol. *185*, 295-302.

Massover, W.H. (2011). New and unconventional approaches for advancing resolution in biological transmission electron microscopy by improving macromolecular specimen preparation and preservation.

Micron *42*, 141-151.

McMullan, G., Faruqi, A.R., Clare, D., and Henderson, R. (2014). Comparison of optimal performance at 300 keV of three direct electron detectors for use in low dose electron microscopy. Ultramicroscopy *147*, 156-163.

Noble, A.J., Dandey, V.P., Wei, H., Brasch, J., Chase, J., Acharya, P., Tan, Y.Z., Zhang, Z., Kim, L.Y., Scapin, G., et al. (2018). Routine single particle CryoEM sample and grid characterization by tomography. Elife *7*, e34257.

Razinkov, I., Dandey, V., Wei, H., Zhang, Z., Melnekoff, D., Rice, W.J., Wigge, C., Potter, C.S., and Carragher, B. (2016). A new method for vitrifying samples for cryoEM. J. Struct. Biol. *195*, 190-198.

Rubinstein, J.L., Guo, H., Ripstein, Z.A., Haydaroglu, A., Au, A., Yip, C.M., Di Trani, J.M., Benlekbir, S., and Kwok, T. (2019). Shake-it-off: a simple ultrasonic cryo-EM specimen-preparation device. Acta Crystallogr. D Struct. Biol. *75*, 1063-1070.

Scheres, S.H. (2012). RELION: implementation of a Bayesian approach to cryo-EM structure determination. J. Struct. Biol. *180*, 519-530.

Stagg, S.M., Lander, G.C., Pulokas, J., Fellmann, D., Cheng, A., Quispe, J.D., Mallick, S.P., Avila, R.M., Carragher, B., and Potter, C.S. (2006). Automated cryoEM data acquisition and analysis of 284742 particles of GroEL. J. Struct. Biol. *155*, 470-481.